



3D printed flow sensor

E.B. (Bernard) Prakken

BSc Report

Committee:

Prof.dr.ir. G.J.M. Krijnen
M. Schouten, MSc
Ing. R.G.P. Sanders
Dr.ir. R.J. Wiegerink

February 2019

007RAM2019
Robotics and Mechatronics
EE-Math-CS
University of Twente
P.O. Box 217
7500 AE Enschede
The Netherlands

3D Printed Flow Sensor

Bernard Prakken

March 12, 2019

Contents

1 Abstract	1
2 Introduction	2
2.1 Context	2
2.2 Related work	2
2.3 Goal	2
2.4 Requirements	2
2.5 Approach	2
3 Conceptual Design	3
3.1 Introduction	3
3.2 Available materials	3
3.3 Printing method	3
3.4 Environment	3
3.5 Measurement method	4
3.6 Concept models	4
3.7 Comparison of models	6
3.8 Conclusion	6
4 Design	8
4.1 Introduction	8
4.2 Mechanical model	8
4.3 Simulations	11
4.4 Conclusion	13
5 Fabrication	16
5.1 Introduction	16
5.2 Samples	16
5.3 Conclusion	18
6 Measurements	21
6.1 Introduction	21
6.2 Measurements	22
6.3 Conclusion	23
7 Results	24
7.1 Introduction	24
7.2 Results	24

7.3 Conclusion	25
8 Conclusion	28
9 Recommendations	29
Bibliography	30

1 Abstract

The use of 3D printing has grown exponentially over the last few years. Individuals are able to print their own designs and products. However, the industry has not yet adopted this innovative production method to its full potential. Products are produced in bulk with lots of waste, causing environmental problems. Even with the production of sensors. This project is therefore focused on producing a functional flow sensor that is fully 3D printed.

In this project a flow sensor is designed to measure the airflow over the wings and/or body of a robot bird. The foremost requirement of this sensor is that it should be produced in a 3D printer and require as little assembly as possible.

Three different models have been designed whereof one design has been produced. This model has the shape of a flat plate with a strain gauge on the front and a strain gauge on the back of the plate. These strain gauges are made of the PI-ETPU conductive material while the largest part of the sensor consists of Ninjaflex. Both these materials are flexible plastics (TPU) which make the sensor act as a deform-able beam.

The produced sensor is able to measure deformations that are equivalent to air flows up to at least 25 m s^{-1} , using the piezoresistive properties of the PI-ETPU filament.

2 Introduction

2.1 Context

The reason for this project is that there is a new technique where conducting materials can be used in a 3D printer. This opens up new possibilities when it comes to electronics. With this technology, it is possible to 3D print conducting networks or circuits into an insulating material, thus opening up the possibility to produce working sensors directly from a 3D printer. This project focuses on the potential of creating a 3D printed flow sensor. This flow sensor could be placed on the body of a bird inspired robot and therefore measure the airspeed passing over the robot.

2.2 Related work

Related projects to flow sensing are research on the filiform hairs of crickets (H Droogendijk and Krijnen (2014)). However, these hairs are designed for a viscous drag, much lower velocities and a high bandwidth. More related work is the research on 3D printed sensors. These projects vary from 3D printed whiskers (B Eijking and Krijnen (2017)) to 3D printed EMG sensing structures (G Wolterink and Krijnen (2017)). These projects have either been dedicated to the sensing of very small flows or on the design of 3D printed sensors. This project will be combining these topics into the design of a 3D printed flow sensor.

2.3 Goal

The goal of this project is to investigate the possibilities to make a flow sensor that can be integrated into a robot wing or body, with the use of 3D printed materials. This way a better understanding of the airflow over a robot is created. The sensor has to measure the airspeed of the bird and will therefore not be designed for measurements of small flow variations.

2.4 Requirements

The most important requirement of the sensor is that the sensor should be 3D printed, making the manufacturing of the sensor an important requirement. The design has to be compatible with the available printer. The next requirement is that the sensor should be functional as soon as it is printed and require the least amount of assembly as possible. The printer that is used for this project is only able to print two different filaments, therefore it is important that the sensor consists of at maximum of two materials. The final requirement is that the sensor should be able to measure flow.

2.5 Approach

The plan is to design a sensor that is based on the flow sensors of animals and nature. First a design selection will be done in order to investigate what types of designs will be best suitable for this sensor. Then the physics around the sensor will be analysed and the different parameters will be calculated. After the analytical model is created, the model will be 3D printed and it will be tested whether it measures a deformation similar to the deformation generated by the air speeds of a bird.

3 Conceptual Design

3.1 Introduction

In this chapter, several conceptual designs of the flow sensor are elaborated on. The pros and cons of the designs are weighed against each other. Three different designs will be examined and inspected: a hair model, a model based on a paddle, and a flat plate model. When comparing the different designs with each other, three leading factors are evaluated: the available materials that can be used for fabrication; the method of 3D printing; and the environment that the sensor will be in.

3.2 Available materials

The final key factor is the materials that are available. The most important material in this project is the PI-ETPU 85-700+ (MSc report Schouten (2017)) with carbon black particles infused. Just like regular TPU, this filament has flexible properties. However, PI-ETPU 85-700+ is a conducting filament that has piezoresistive properties. Meaning that the resistance of a printed part changes when it is bend or stretched in a different shape. These particles form conducting networks in the TPU. When the material is stretched, the carbon network within the TPU changes layout. This change in layout can then be measured and related to the additional length gained by stretching. Next to conducting materials, there are also non-conducting TPU materials: Ninjaflex (NinjaTek (2019)) and X60 (MakeShaper (2018)). Both these materials are flexible materials. However the X60 is more flexible than the Ninjaflex. Ninjaflex has a flexibility rating of 85 shore A, where X60 is a 60 shore A filament. This is a rating that describes the flexibility of a material or shore hardness.

3.3 Printing method

When designing a sensor, the model should be in line with the method of production. Meaning that the production technique is actually capable of producing the desired model. However, in this scenario, the production technique is already fixed, namely with the use of a Flashforge 3D printer (Flashforge (2019)). This printer is able to print two different materials in the same process. The printer has a nozzle diameter of 400 μm for regular TPU (thermoplastic polyurethane) and a diameter of 600 μm for conductive TPU. This larger nozzle diameter has to do with the flow of the carbon black particles through the extruder. If the nozzle size is set at the same diameter as of the regular TPU, the carbon particles will clog the nozzle and extruder, which would ruin the print. These nozzle diameters therefore determine the minimum resolution the sensors can be build with. The maximum size of the prints is bounded by the size of the heated bed, which determines the maximum transversal dimensions, and the maximum print height of the 3D printer, which limits the maximum height of the prints..

3.4 Environment

The next important factor is the environment of the sensor. This is the location of the sensor and the circumstances in which the sensor will have to operate. In this case, the sensor should be designed in such a way that it can be positioned on the body and wings of a mechanical bird, the Robird [3] by Clear Flight Solutions. The Robird in question is based on a peregrine falcon (Figure 3.1). A peregrine falcon is able to reach velocities of about 102 m s^{-1} during diving. The Robird, however, is able to fly at speeds up to 16 m s^{-1} . The flow sensor should be able to measure these velocities, but should not hinder the Robird to reach these speeds. Therefore it is important that the sensor does not introduce a significant change to the aerodynamics of the Robird.



Figure 3.1: Robird by Clear flight solutions (2018)

3.5 Measurement method

When designing a flow sensor with conductive TPU, there are multiple ways of measuring the desired flow or pressure. A possibility is to print multiple conducting lines close to each other in the structure of the sensor and measure the change in capacity when the structure is bend or deformed. Another method of measuring a flow or pressure is to integrate loops of conducting material in the structure where the change in resistance is measured. This utilises the piezoresistive properties of the filament. When such a loop is stretched, the resistivity of the material changes and therefore the resistance of the loop altered. These conductive loops should then be placed in the structure, positioned in the direction where the deformation is maximum. Using resistive loops requires a less sophisticated measurement setup than measuring the capacitive changes in the structure.

When using a single loop of conducting material in a sensor, the measured resistance would be $R + \Delta R$. Where R is the resistance of the sensor when it has no force acting upon it and ΔR is the change in resistance. So ΔR can only be calculated when R is known. This would be fine if the materials in the sensor always return to their original shape. However, this is not the case. When TPU endures a pressure or force for a while, the structure won't go back to its original form when the pressure/force is gone. This creates a drift in the measurements and would lead to an inaccurate flow value. To cope with this drift, a second loop can be added to the sensor. This allows for a differential measurement setup where only the difference in resistance between the loops is computed. Doing so, eliminates the need of having a reference to the resistance in the original form of the sensor. An assumption is therefore made that with the use of a differential measurement setup, the shape drift in both loops is equal. Meaning that the change in shape of the structure when in neutral position is the same for each conductive loop. It is important that these strain gauges encounter enough strain for a wind speed of 16 m/s to be detected. The resolution of the sensor is therefore important to the design. If the resolution of the sensor is not sufficient to detect this flow, then the sensor would not meet its requirements.

3.6 Concept models

As said, a total of three concept models have been created for this sensor. The first concept, *concept 1*, is based on an animal hair. In particular the hairs on the tail of a cricket (called filiform hairs) and mammalian whiskers, keeping aside the difference in size, functionality and performance. There are multiple researches done when it comes to hair sensors which are scaling from nanometer long hairs, the filiform hairs (H Droogendijk and Krijnen (2014)), to a few decimetres, whiskers (B Eijking and Krijnen (2017)). With the use of their filiform hairs, crickets are able to sense low-frequency flows. Each hair can primarily move in one plane, but due to the hundreds of hairs in different orientations on the its tail, the cricket is able to sense where the predator or object is coming from. Whiskers however work very different. Whiskers are used to detect object or forces by direct contact and are therefore much larger than filiform

or 'tactile' hairs. Each hair can sense the amount of force, the direction of this force as well as the point of action of the force on the whisker (Mitra Hartmann (2018)). This concept model, seen in Figure 3.2, measures the amount and direction of flow along its bending direction. As seen in the figure, the loops of conducting material (shown in black) are based at the bottom of the sensor. The base of the sensor is fixed and the top of the hair is subject to the airflow.

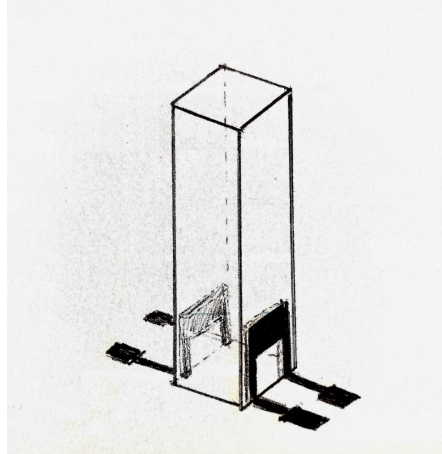


Figure 3.2: Hair concept model

The second concept model, a version of this is shown in Figure 3.3, is in essence a flat plate perpendicular to the flow of air. This model has the same principles as *concept 1*, however this model is much wider. Meaning it will endure substantially more drag, which is not necessary a bad property as it also gets more sensitive. Due to its wider frame, it is easier for the printer to produce such a model. A flat plate model also enables more space for the E-TPU loops.

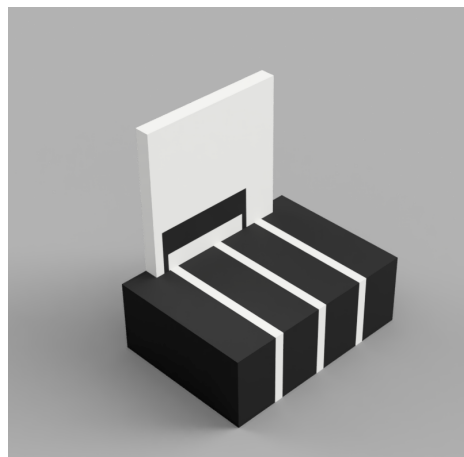


Figure 3.3: Flat plate concept model

And finally *concept 3*, a concept model inspired by a paddle. This sensor, seen in Figure 3.4 has a small base and a large frontal surface area. Allowing the sensor to bend more than concept 1, but with less flow needed. Logically, this concept does induce more drag than the model of a hair, but not as much as a flat plate. The round top of the model keeps the sensor streamlined, which is an aerodynamic advantage. To get a sensor with reasonable sensitivity it is a requirement to get sufficient drag-force on the structure. Eventually, the optimisation is in getting as much bending moment as possible for a given drag-force.



Figure 3.4: Paddle concept model

3.7 Comparison of models

	Printing method	Environment
Concept 1	+ easily printed sideways - requires high accuracy	+ proven concept by nature + creates little drag
Concept 2	++ easily printed flat + requires least accuracy	+ - creates much drag
Concept 3	- hard to print due to roundness - supports needed	+ creates little drag + high sensitivity

Table 3.1: Trade-offs between the different concepts

When comparing these concepts, seen in table 3.1, it's clear that a paddle model is hardest to produce. The round top is hard to produce with flexible materials and rigid supports are needed for the smaller base to be printed. Next to that is the fact that the larger top creates a low resonance frequency. This can be a disadvantage when the flow over the sensor is alternating. The measurements of the sensor become very inaccurate when the sensor starts resonating. Considering the printing method, a flat plate model is easiest to print. The hair model has very little surface area to integrate conducting loops and would be incompatible with the minimum dimension requirements of the printer. However, when looking at the environment of the sensor, the concept 3 is the most suitable model. The large cylinder on the small base makes the sensor bend more with less flow. This increases the responsivity of the structure. On the second place stands the hair based model. This model creates very little drag and is already used in a variety of flow sensing applications, such as in flow sensing with filiform hairs. When it comes to the environment of the sensor, the worst concept is concept 2. The large frontal area creates a lot of drag of the robot. The flow over the wing gets deformed, which decreases the efficiency of the robots flight. However, the same accounts for the other concepts. When it comes to the choice of materials, all concept models are realisable with both Ninjaflex and X60.

3.8 Conclusion

The flat plate model is the most realisable model of the three concepts. This sensor would create more drag than the other models, due to its large frontal area, but it has a realistic shape suitable for production on a 3D printer. The other two concepts have more efficient properties giving fewer drag to the bird, but these are not printable with the current 3D printer infrastructure. The wide face of the sensor is easy to print and requires no additional supports. The large

face enables more options for measuring the conducting loops of E-TPU. In the next chapter this model will be explained and elaborated on.

4 Design

4.1 Introduction

In this chapter an explanation of the design choices that have been made will be given. The mechanical model is analysed and simulations of this model give an approximation to the properties of the sensor. The flat plate model consists of two similar conductive loops, which stretch and compress when a flow is acting upon the sensor.

4.2 Mechanical model

The model that is used is the flat plate model. Due to the presumed uniform flow that interacts with the sensor, the y-dimension of the sensor can be taken arbitrarily, making the mechanical model of this sensor best represented as an upright cantilever. A cantilever is a beam which has a fixed base on one end, whereas the other end is free (seen in figure 4.1). In this figure, ω is the uniformly distributed load per unit length on the sensor, l is the length of the beam and δ_{\max} is the displacement in the x direction at the end of the beam.

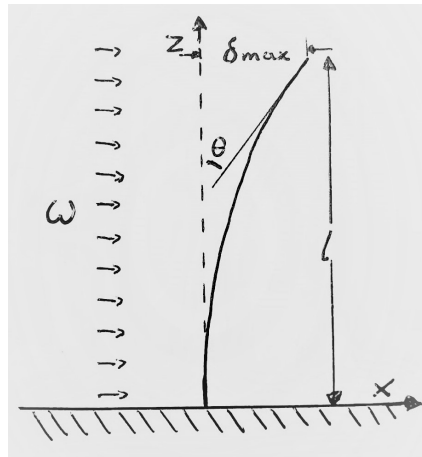


Figure 4.1: A cantilever beam representation of the flat plate sensor model.

4.2.1 Beam equations

For small deformations, the displacement of the beam can be approximated with the Euler-Bernoulli beam equation (Gere (2012)). These equations describe the relation between the beam's deflection and the applied load. Equation 4.1 is the Euler-Bernoulli equation for the cantilever shown in figure 4.1:

$$\frac{d^2}{dz^2} \left(EI \frac{d^2 x}{dz^2} \right) = \omega \quad (4.1)$$

For this cantilever, the equation can be simplified to equation 4.2 for the displacement in the x -direction, and in equation 4.3 for the angle of deflection both in terms of z (Gere (2012)):

$$x = \frac{\omega z^2}{24EI} (z^2 + 6l^2 - 4lz) \quad (4.2)$$

$$\theta = \frac{\omega z}{6EI} (z^2 + 3l^2 - 3lz) \quad (4.3)$$

These equations show the displacement and the angle of deflection of the cantilever at any point over the beam, where z is the distance over the beam to the base and l is the total length of the beam. E is the Young's modulus of the material. This modulus represents the flexibility

or stiffness of the material. In this case the sensor consist primarily of Ninjaflex filament, so for modelling the young's modulus of the Ninjaflex is used for the simulations. Ninjaflex has a modulus of $E = 12 \text{ MPa}$ (NinjaTek (2018)). In reality the overall Young's modulus of the Sensor will be larger than 12 MPa , due to the integrated PI-ETPU. This filament has a higher modulus than the Ninjaflex, caused by the non-flexible carbon particles in the filament. I is the second moment of inertia of the beam (Beer (2013)). This is a property of an objects shape, that predicts the deflection or displacement of this object. For a rectangular area it can be represented as equation 4.4, where A is the area of the intersection of the beam and b & d are the width and thickness respectively .

$$I = \iint_R y^2 dA = \int_{-\frac{b}{2}}^{\frac{b}{2}} \int_{-\frac{d}{2}}^{\frac{d}{2}} y^2 dy dx = \int_{-\frac{b}{2}}^{\frac{b}{2}} \frac{1}{3} \frac{d^3}{4} dx = \frac{bd^3}{12} \quad (4.4)$$

With the use of equation 4.2 it is also possible to calculate δ_{\max} by calculating x for $z = l$:

$$\delta_{\max} = \frac{\omega l^2}{24EI} (l^2 + 6l^2 - 4ll) = \frac{\omega l^4}{8EI} \quad (4.5)$$

δ_{\max} is the maximum deflection at the end of the sensor and may be useful for initial measurements.

4.2.2 Strain

In order to calculate the change in resistance by means of the applied load, the fiber strain on the strain gauges of the sensor is to be determined. Figure 4.2 gives an illustration of the induced strain caused by bending of the sensor. The black bars represent the PI-ETPU strain gauges of the sensor. When the sensor is bend by the applied load, an angle θ (in radians) is created. This angle is the same θ as given in figure 4.1. From this schematic drawing, it is clear

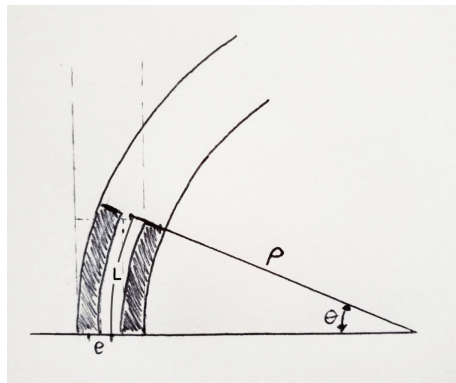


Figure 4.2: A schematic representation of the strain in the conductive PI-ETPU

that for small θ the length L of the strain gauge can be calculated as follows:

$$L = \rho\theta \implies \rho = \frac{L}{\theta} \quad (4.6)$$

Where ρ is the radius of the approximated circle created by the load. This circle only holds for small displacements near the base of the sensor. In figure 4.2 e represents the distance from the neutral axis of the beam to the center of the strain gauge. The difference in length between the center of the beam and the center of the left strain gauge is denoted as ΔL . This also implies that:

$$\frac{L}{\rho} = \frac{\Delta L}{e} \implies \frac{\Delta L}{L} = \frac{e}{\rho} \implies \frac{\Delta L}{L} = \frac{e\theta}{L} \quad (4.7)$$

Combining equation 4.7 with equation 4.3 gives:

$$\varepsilon = \frac{\Delta L}{L} = \frac{e\omega z(z^2 + 3l^2 - 3lz)}{6EIL} \quad (4.8)$$

However, in this equation, z is the position on the upright cantilever where the strain gauge is located. Therefore integrating ε over an interval from 0 to L gives the desired strain, which leads to the following equation:

$$\varepsilon_L = \frac{1}{L} \int_0^L \frac{e\omega z(z^2 + 3l^2 - 3lz)}{6EIL} dz = \omega \cdot \frac{e(L^2 + 6l^2 - 4lL)}{24EI} \quad (4.9)$$

This shows that the relation between the difference in length and the applied load is linear for small deflections. This was as expected, since the assumption is made that the load is position independent. However there is a flow (in ms^{-1}) applied to the sensor, rather than a load (in Nm^{-1}). To convert this, the load can be written as a function of the flow velocity (NASA (2015)):

$$\omega = \frac{F_D}{l} = \frac{\frac{1}{2}C_D D v^2 A}{l} = \frac{\frac{1}{2}C_D D v^2 bl}{l} = \frac{1}{2}C_D D v^2 b \quad (4.10)$$

In this equation, F_D is the drag force upon the sensor, C_D is the drag coefficient of the the sensor shape, D is the density of the fluid, v is the flow velocity and A is the frontal surface area of the sensor. The drag coefficient of a flat plate positioned perpendicular to the flow is equal to $C_D = 1.28$ (NASA (2013)). The density of air at a temperature of 15 degrees can be taken as $D = 1.225 \text{ kg/m}^3$ (IPFS (2017)). These constants, combined with equations 4.10 and 4.9 give a relation between the change in length of the left strain gauge and the flow velocity upon the sensor:

$$\frac{\Delta L}{L} = \frac{1}{2} (1.28)(1.225) v^2 b \cdot \frac{e(L^2 + 6l^2 - 4lL)}{24EI} \quad (4.11)$$

Which can be rewritten as:

$$\frac{\Delta L}{L} = v^2 \cdot \frac{(1.28)(1.225)be(L^2 + 6l^2 - 4lL)}{48EI} \quad (4.12)$$

The same thing can be done for equations 4.10 and 4.5:

$$\delta_{max} = \frac{(\frac{1}{2}C_D D v^2 b)l^4}{8EI} \implies \delta_{max} = v^2 \frac{(1.28)(1.225)bl^4}{16EI} \quad (4.13)$$

It is important to note that equation 4.12 only holds for the strain gauge that is extended. The other strain gauge is compressed and will therefore have a negative $\Delta L/L$. This can be confirmed since the distance from the center of the beam to the center of the strain gauge is defined as $-e$ for the compressed strain gauge. Therefore a minus sign will show when compressing the strain gauge.

When performing the measurements, an actuator is used rather than a wind tunnel. However, an actuator is not able to distribute a load over the length of the model, regardless of the shape of the bend. To solve this, an analogy has to be made from a model where the load is uniformly distributed to a model where a force is applied only to the free end of the model. To do so, the Euler-Bernoulli equation for the angle and the maximum deflection have been rewritten for a beam with a concentrated load:

$$\theta_c = \frac{Pz}{2EI} (2l - z) \quad (4.14)$$

$$\delta_{maxc} = \frac{Pl^3}{3EI} \quad (4.15)$$

When setting equation 4.15 equal to the maximum deflection of a uniformly distributed load 4.5, the equivalent load can be calculated:

$$\frac{Pl^3}{3EI} = \frac{\omega l^4}{8EI} \implies P = \frac{3}{8}\omega l \quad (4.16)$$

This can then be implemented in equations 4.3 and 4.7:

$$\frac{\Delta L}{L} = \frac{e\theta_c}{L} = \frac{ePz}{2EIL}(2l-z) = \frac{3e\omega lz}{16EIL}(2l-z) \quad (4.17)$$

Then, following the same integration steps as earlier:

$$\frac{\Delta L}{L} = \frac{1}{L} \int_0^L \frac{3e\omega lz(2l-z)}{16EIL} dz = \omega \cdot \frac{el(3l-L)}{16EI} \quad (4.18)$$

$$\frac{\Delta L}{L} = v^2 \cdot \frac{(1.28)(1.225)bel(3l-L)}{32EI} \quad (4.19)$$

This can then be rewritten as a function of the maximal deflection:

$$\frac{\Delta L}{L} = \delta_{max} \cdot \frac{e(3l-L)}{2l^3} \quad (4.20)$$

Equation 4.20 can now be used to transform a given deflection to the end of the model to the strain in the strain gauges.

4.3 Simulations

4.3.1 Boundary layer

When an airflow is subject to a wing or a flat plate parallel to the flow of air, a boundary layer is generated. A boundary layer is a layer of air over the wing or plate that has different airflow consistency than free flowing air. The air in a boundary layer differs from no velocity at the surface of the wing to 99% of the free flow speed u_0 at the edge of the boundary layer. This non-linear change in flow may doubt the correctness of the model taken in figure 4.1.

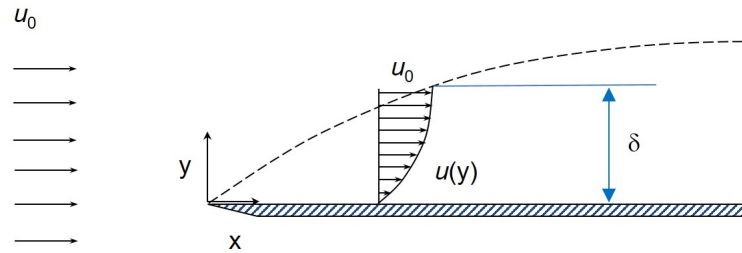


Figure 4.3: A schematic representation of the boundary layer over a flat plate [REF]

For laminar flow, meaning that the fluid flows in parallel layers, the thickness of the boundary layer can be approximated using the Blasius solution (Schlichting (1960)):

$$\delta = 4.91 \sqrt{\frac{\nu x}{u_0}} \quad (4.21)$$

In this equation, ν is the kinematic viscosity of the medium. Which for air is $\nu = 1.426 \times 10^{-5} \text{ ms}^{-2}$ at 10°C (Engineering Edge (2000)). x is the distance from the edge of the flat plate. Plotting this boundary layer thickness for a velocity of 16 ms^{-1} and a typical wing length of a peregrine falcon of about 18 cm long gives figure 4.4 .

It is important to note that this simulation is done over a flat plate, rather than a wing. The cross section shape of an actual wing asks for a far more complex calculation. Therefore a flat

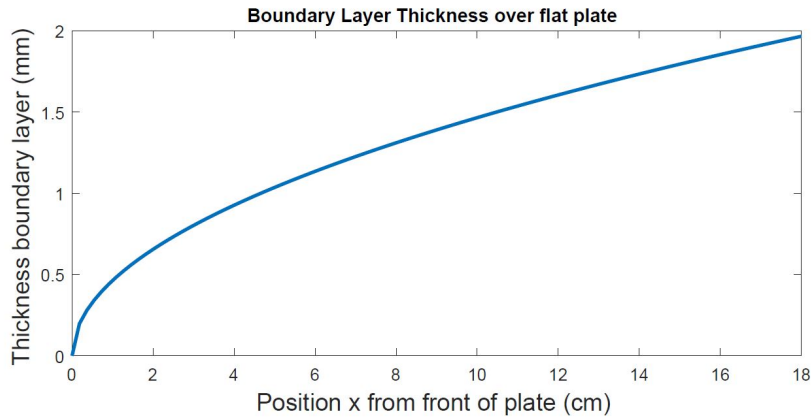


Figure 4.4: Boundary layer thickness for a flat plate of 18 cm

plate simulation is performed to investigate the significance of a boundary layer on the sensor. From figure 4.4, it is clear that the boundary layer over the flat plate is less than 2 mm thick. As long as the sensor is significantly larger than 2 mm, this boundary layer can be negligible. This also indicates the correctness of the model shown in figure 4.1 for velocities of at least 16 m s^{-1} .

4.3.2 Flow simulations

To simulate the change in length of the sensor, three sizes samples have been taken:

- A sample of $10 \times 10 \times 1$ mm (lxbxd), noted as small model.
- A sample of $20 \times 20 \times 2$ mm (lxbxd), noted as large model.
- The final sample of $20 \times 20 \times 1.2$ mm (lxbxd), noted as the final model.

In these simulations the strain gauge length/height is set at 10% of the height of the sensor, and e is taken to be 0.8 mm for the large model and taken 0.4 mm for the small and the final model. For this simulation a sweep is done for the flow velocity, starting at 0 m/s and ending at 32 m/s. This is to ensure that the resolution of the sensor is able to measure the basic flight speed of 16 m/s of the Robird (RaM (2018)). Another reason that velocities higher than 16 m/s are simulated is that the airflow over the body of the Robird may be much faster.

As shown in 4.5, both in the small and the large model the strain gauges extend the same amount. However, in the final model, the strain gauge extends much more. This result is not unexpected as b , l and L are all multiplied by a factor two (and therefore adding up to a factor of 8) in the numerator of strain equation 4.12, where in denominator the second moment of inertia is also multiplied with a factor of $2 * 1.2^3 = 3.456$. Stating this, it is also clear that as long as the sensor is scaled evenly in all dimensions, the strain in the strain gauges will not be affected. It is clear from the strain equation 4.12, that the best way to enlarge the strain in the sensor is to decrease the second moment of inertia, thus scaling the thickness down in comparison to the other dimensions, since the thickness is taken by a power of three. This also reduces the distance of the train-gauge to the neutral axis, e , which will lead to smaller signals.

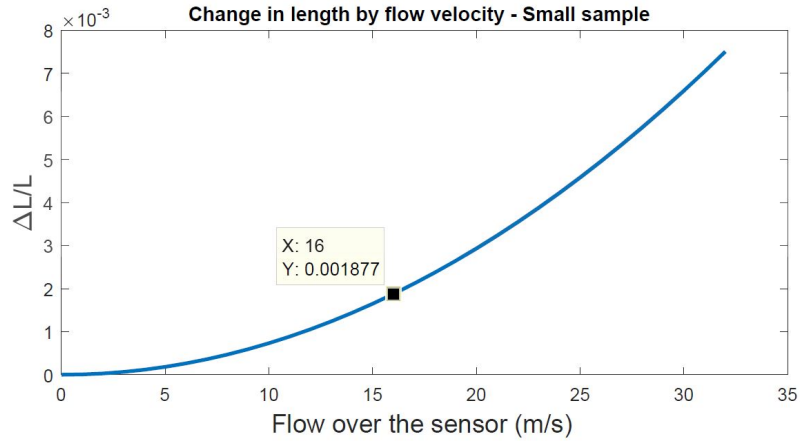
4.3.3 Deflection

For the simulation of the displacement in the sensor (shown in figure 4.6) the same three models have been taken. As with the fiber strain simulation, the flow velocity has been swept from 0 to 32 m/s. From these plots, it becomes clear that the offset as function of the flow velocity is not a linear relation. As equation 4.13 already shows, the relation between δ_{\max} and v is

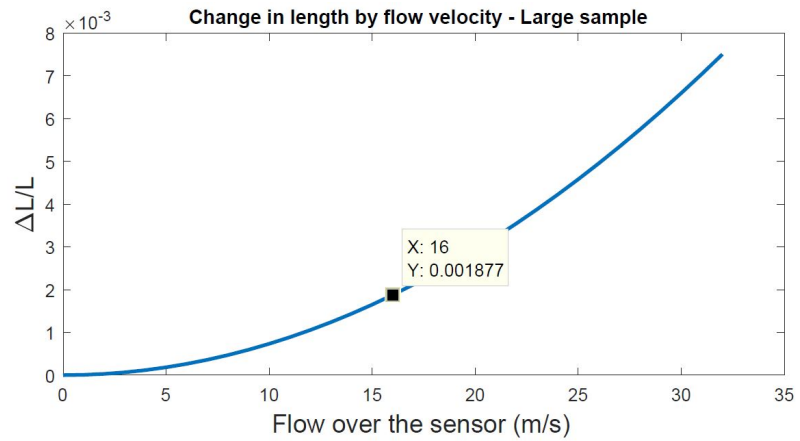
quadratic. Another remark seen from the plots is that there is a factor 2 difference between the maximum deflection of the small model and the large model. This can be related by the fact of the dimensions of the sensor are taken into account once more in the numerator of equation 4.13 than in the denominator. As with the strain in the models, the final model also has a lot more deflection than the other two competitors. Due to the thin frame of the sensor compared to the other two sensors, the second moment of inertia is only scaled by 3.456, while the numerator is scaled with a factor 32. This creates a deflection that is almost ten times bigger than the small model.

4.4 Conclusion

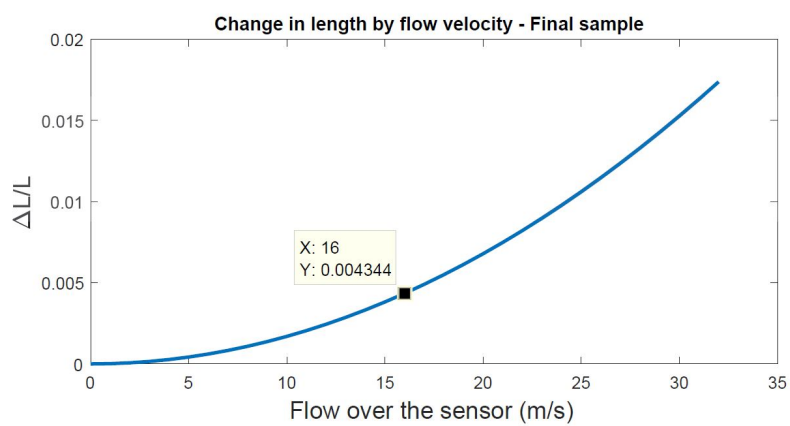
When combining the information gained from both the simulation of the fiber strain and the simulation of the maximum deflection of the models, some important factors have become clear. The relation between the dimensions of the sensor is essential. In particular the thickness of the sensor. When increasing the frontal surface of the sensor, while remaining a small thickness will result in a higher resolution. The drawback to this non-uniform scaling is that the sensors maximum flow velocity will decrease. The maximum deflection of the sensor has an absolute limit and this will be reached at a lower flow velocity. Another important note to keep in mind is that, in this report, no research is done in the effects a larger sensor will have on the airflow and the physics of a wing.



(a) Fiber strain for the small sensor.

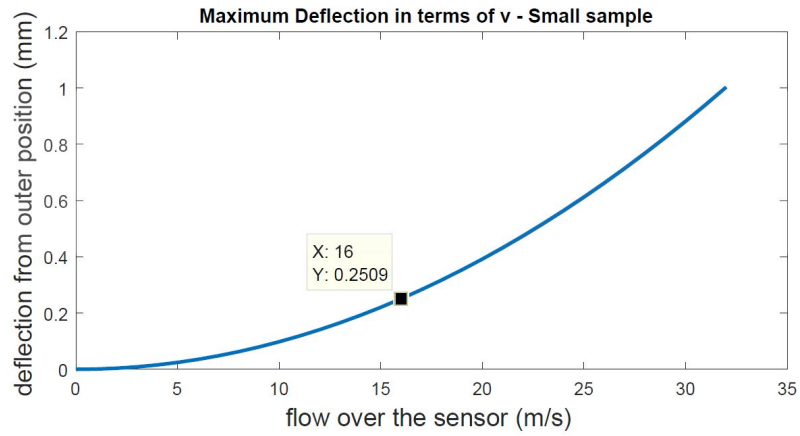


(b) Fiber strain for the large sensor.

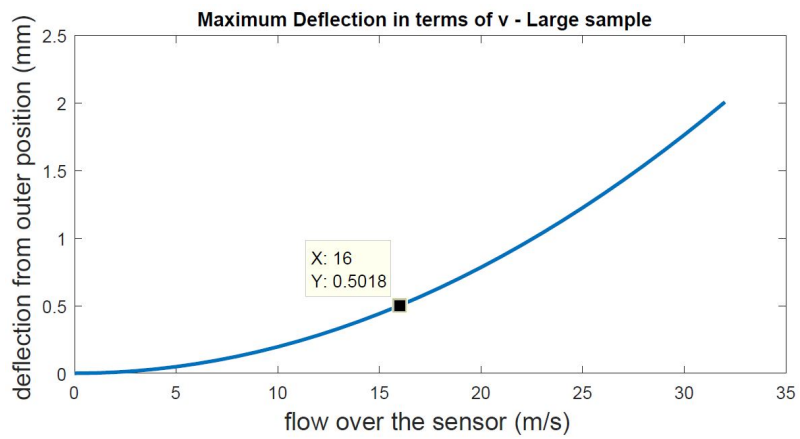


(c) Fiber strain for the final sensor.

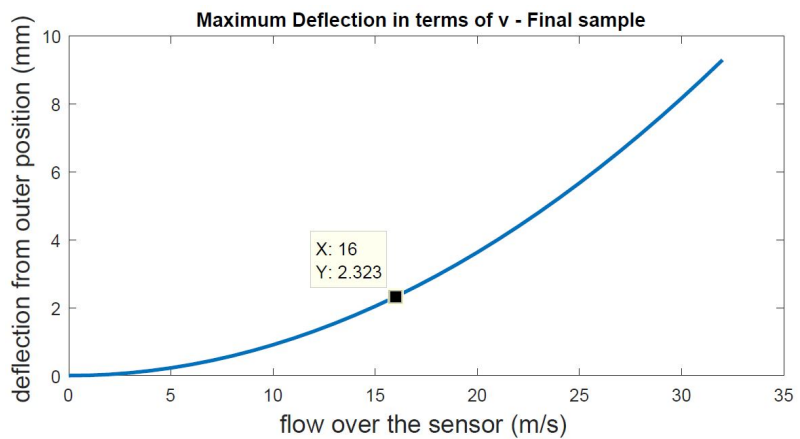
Figure 4.5: Fiber strain as function of the flow velocity.



(a) Deflection of the small model.



(b) Deflection of the large model.



(c) Deflection of the final model.

Figure 4.6: Maximum deflection as function of the flow velocity.

5 Fabrication

5.1 Introduction

During the production phase of the project, multiple designs have been printed. For printing these designs, the Flashforge Creator Pro 3D printer is used. As stated in chapter 3, this printer is capable of printing two different materials in one print. While printing, the left extruder was loaded with Ninjaflex (NinjaTek (2019)) and the right printer was loaded with the PI-ETPU filament (Schouten (2017)). In total a number of three different designs have been produced, each descending from their predecessors:

- **Model 1:** This is the same model as shown in chapter 3 figure 3.3. With this model, the loops are placed asymmetric. Meaning that the measurement loops are not aligned in front of each other. This design choice is made to keep as much space for the connectors to be placed. Doing so gives the ability to apply the connectors to either the front, back or bottom of the sensor. To increase the connector pads surface more, the connector pads have been extended.
- **Model 2:** This sensor model, presented in figure 5.1, is a redesign of *model 1*. In this model, the measurement loops have been positioned directly in front of each other. To ensure that there is no connection made between the connector pads of the same loop, a larger gap is of Ninjaflex is added to the bottom part of the sensor. The connector pads have been moved to the bottom and side edges of the sensor. Another design choice made in *model 2* is that there is a solid layer of Ninjaflex in between the front and the back measurement loops, providing an insulator between the loops.

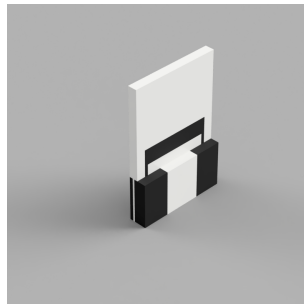


Figure 5.1: Model 2

- **Model 3:** Model 3 has nearly the same dimension as *model 2*. However, to ensure that the broad top part of the measurement loops has a low resistance value, the measurement loops have been narrowed down. Additional to this, a ring of Ninjaflex has been added to around the sides of the sensor, keeping the chance of PI-ETPU leaking over the edges of the sensor and connecting the front measurement loop to to the loop at the back. This model is presented in figure 5.2.

5.2 Samples

In total, a number of 11 samples have been produced for this project. Each testing the capabilities of the Flashforge printer. All samples can be seen in image 5.4 and 5.5.

The first two "generations" of samples are based on *model 1*. The first-generation samples were printed with a layer height of 0.1 mm. As seen in the figures, the quality of these samples is very

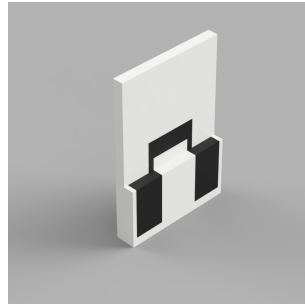


Figure 5.2: Model 3

bad. The PI-ETPU has been mixed in with the Ninjaflex at places only Ninjaflex should have been. These samples have a plate height (the upright part of the sensor) of 10 mm, a width of 10 mm and a thickness of 1 mm. There is a 'connector tower' at the bottom of the samples, which was designed to give the sensor more stability and to make sure that the connector pads would not deform by the airflow. The second generation samples were printed with a layer height of 0.2 mm. This clearly mixed less ETPU into the Ninjaflex. The small sample has the same dimensions as the samples from the first generation. The second print is scaled twice the size of the other sample. This was a test to see whether the print quality would go up, which is definitely the case. There is much less mixture between the two filaments and the strain gauges are more defined.

Sample "generations" three and four are based on *model 2*. The large prints of *model 2* show better defined strain gauges than the previous models. The small print is has the same dimensions as the prints of generation 1. This however, is also the last print with these dimensions. It was clear that the printer accuracy is not high enough to create prints at these sizes, therefore new prints were made with only the height and the thickness scaled. This resulted in samples with plate dimensions of 20 mm × 20 mm × 1 mm. This allowed for prints with less mixture of the materials, while enhancing the flexibility of the sensor. The difference between generation 3 and 4 is that the heating bed temperature has been decreased from 60 °C to 25 °C and a bottom print-layer of double the thickness. This allowed for the bottom of the print to cool off more and restrain the running of the filaments. Another change that has been made in between these samples is that the printing speed has been reduced by half. Where the printing speed was 100 mm/s, has been set to 50 mm/s. This resulted in a more controlled flow of filament with fewer print errors. As seen in figure 5.4.

The final prints have been based on *model 3*. These prints where of the highest quality of all samples. The infill in these prints has been rotated by an angle of 45°, resulting in a uniform distribution of filament within the strain gauges. The infill beforehand was all angled alternating at −45° or 45°. The final print that was actually used for measurements has two differences from the samples of generation 5. The final print has an increased thickness of 1.2 mm, rather than the original thickness of 1.0 mm. This allowed for a print with three 0.4 mm layer sections within the print: a strain gauge, an insulating layer and another strain gauge. The other enhancement was to remove the 'connector tower' from the bottom of the sensor, leaving the sensor with a connector pad with the same thickness of 1.2 mm as the measurement section of the print. Doing so resulted in a print with a resistance of 0.9 MΩ from the front strain gauge to the back strain gauge. Where the strain gauges themselves have a resistance of 1.78 kΩ for the front loop and 1.58 kΩ for the back loop. A schematic drawing of the strain gauges in the final print is given in figure. The dimensions are denoted in millimetres. The parameters mentioned above are presented in tables 5.1 and 5.2.

Model	Gen.	Layer Thickness (mm)	First layer (mm)	Speed (mm/s)
1	1	0.1	0.1	100
	2	0.2	0.2	100
2	3	0.2	0.2	100
	4	0.2	0.4	50
3	5	0.2	0.4	50
	final	0.2	0.4	50

Table 5.1: Table with the mentioned parameters of the prints.

Model	Gen.	Bed Temp (C)	Infill Angles	Connector Tower	Thickness (mm)
1	1	60	-45, 45	yes	1.0
	2	60	-45, 45	yes	1.0, 2.0
2	3	60	-45, 45	yes	1.0, 2.0
	4	25	-45, 45	yes	1.0
3	5	25	0, 90	yes	1.0
	final	25	0, 90	no	1.2

Table 5.2: Table with the mentioned parameters of the prints.

5.3 Conclusion

The fabrication process was highly dependent on the capabilities of the Flashforce Creator Pro 3D printer. Mainly for the size of the sensor, the printer accuracy was a leading factor. If, in the future, a better printer is used for this process, the sensor can be scaled down. The design of the sensor is also a key factor for the quality of the final print. As seen from the images 5.4 and 5.5, the earlier designs (*models 1 and 2*) were not compatible with either the accuracy of the 3D printer or the filaments that were used.

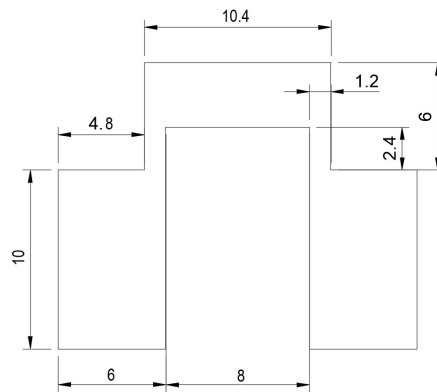
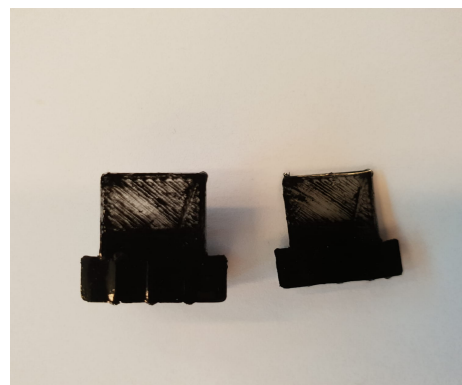


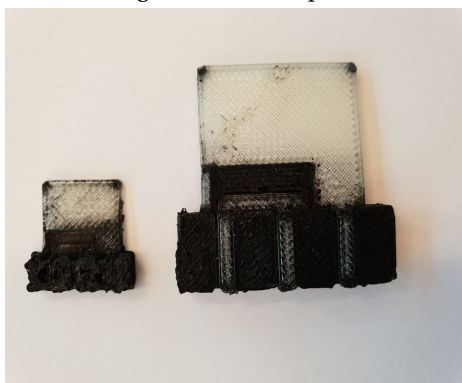
Figure 5.3: Schematic drawing of one strain gauge.



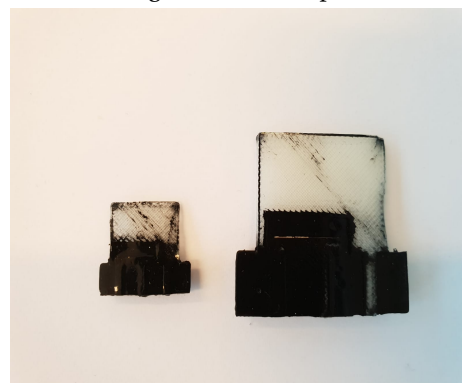
(a) First generation samples, front side.



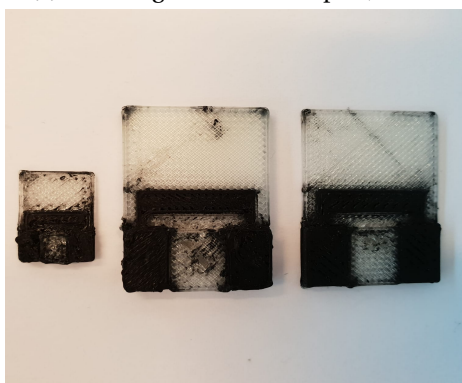
(b) First generation samples, rear side.



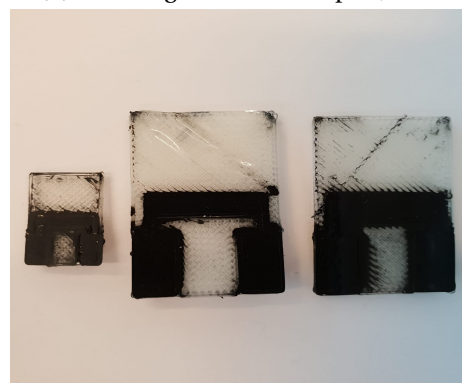
(c) Second generation samples, front side.



(d) Second generation samples, rear side.

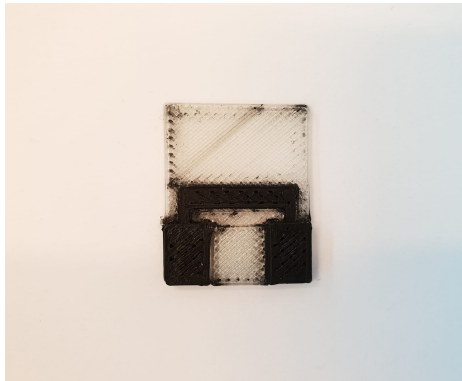


(e) Third generation samples, front side.

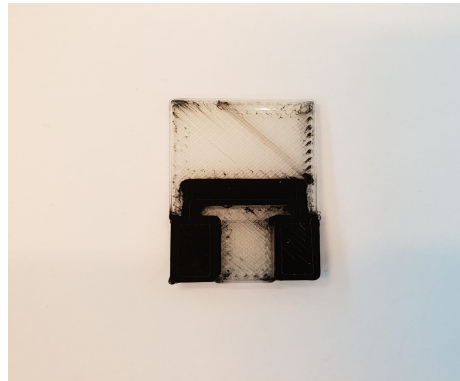


(f) Third generation samples, rear side.

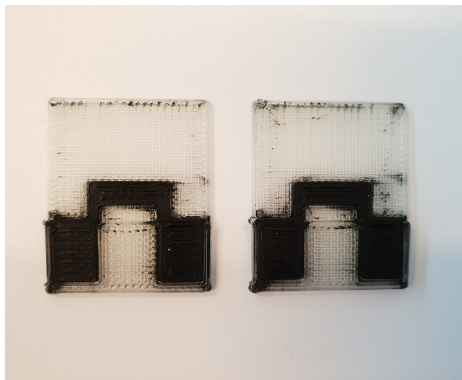
Figure 5.4: The first three generations of sample sensors.



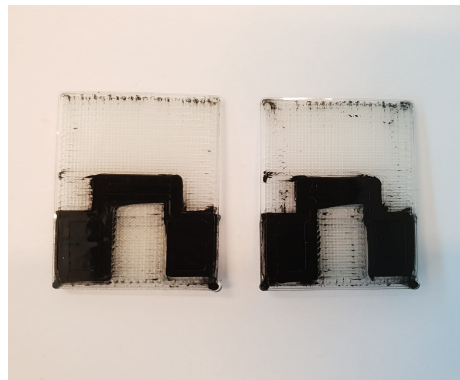
(a) Fourth generation sample, front side.



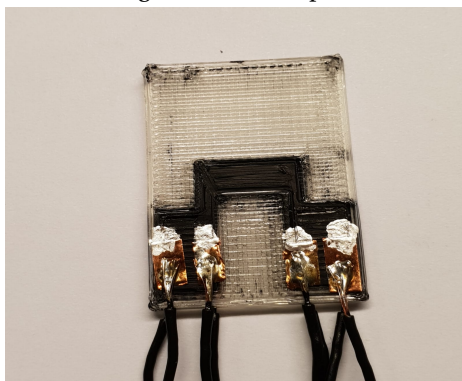
(b) Fourth generation sample, rear side.



(c) Fifth generation samples, front side.



(d) Fifth generation samples, rear side.



(e) Final sample sensor, front side.



(f) Final sample sensor, rear side.

Figure 5.5: Final generations of sample sensors.

6 Measurements

6.1 Introduction

For the measurement setup, a voice coil actuator is used in order to induce an excitation of the sensor. This voice coil actuator, or SMAC actuator (SMAC Moving Coil Actuator (2019)), is used as source to create an offset to the end of the sensor. As shown in the simulations, the flow can also be measured by giving a sensor offset in the direction of the airflow. The ideal measurement setup would be to utilise a wind tunnel. However, due to the poor availability of such a tunnel, an actuator alternative is used for these measurements. The measurement setup that was used is as follows:

- Each strain gauge is equipped with 4 wires to perform a 4-point measurement. These wires are soldered to a piece of copper tape that is stuck on the connector pad of the sensor. To decrease the resistance of the connection, a few drops of silver ink are used link the copper to tape to the connector pads, as seen in picture 5.5e and picture 5.5f.
- The outer wires on the connector pads are connected to a HP E3631A current source and the inner wires connect to an oscilloscope (Analog Discovery 2 (Digilent (2018))) that measures the voltage between the wires, with the use of 'Waveforms' software (Digilent inc (2019)) . The 4-point measurement ensures, due to the high impedance of the oscilloscope, that only the actual voltage over the piezoresistive material is measured.
- For all measurements, two DC current sources (HP E3631A) have been set to 1 mA as input for both strain gauges.
- The fabricated sensor is placed sideways in a fixed position. The bottom part of the sensor is clamped between paper cloth and a rigid plastic clamp, as shown in pictures 6.1.
- To the end of the SMAC actuator, a piece of plexiglass is mounted. This plexiglass has a notch to hold the free end of the sensor. This notch allows for the actuator to both push and pull the free end of the sensor, therefore giving it a positive and negative deflection.
- All measurements have been performed at a sampling rate of $F_s = 50$ Hz. This eliminates any form of 50 Hz distortion in the measured signal, due to the Nyquist criteria (Grenander (1959)). By taking a sample frequency of 50 Hz, the 50 Hz distortion signal gets mirrored over $F_s/2 = 25$ Hz and mapped at 0 Hz, thus removing the distortion.

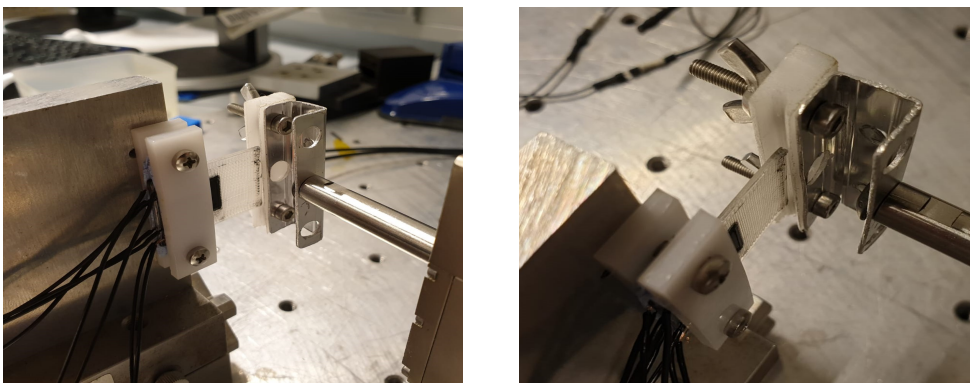


Figure 6.1: The used measurement setup.

6.2 Measurements

The measurements that are performed have been saved as .mat files for the actuator data and the data measured by the Analog Discovery 2 has been saved as .csv files. These files are later processed with the use of Matlab (MathWorks (2018)). This allowed to produce multiple plots with the same measured data. To synchronise the signals of the measurement with the signal from the SMAC actuator, an extra pulse is given to the actuator at the start of the measurement to manually time the signals.

6.2.1 Actuator measurements

In figure 6.2, the raw measurements of both strain gauges is presented. The upper plot in the figure represents the measured resistance of the front strain gauge and the orange plot represents the rear strain gauge. What is important to note is that these measurements are the total resistance of a single strain gauge, thus presenting $R + 2\Delta R$ rather than $\frac{\Delta R}{R}$. The reason for $2\Delta R$ is due to the two measurement strips within each strain gauge. At the bottom plot, the offset given by the SMAC actuator with respect to the time is given. For this measurement, the SMAC actuator has been set to move in a sine from -6 mm to 6 mm deflection at a frequency of 0.5 Hz.

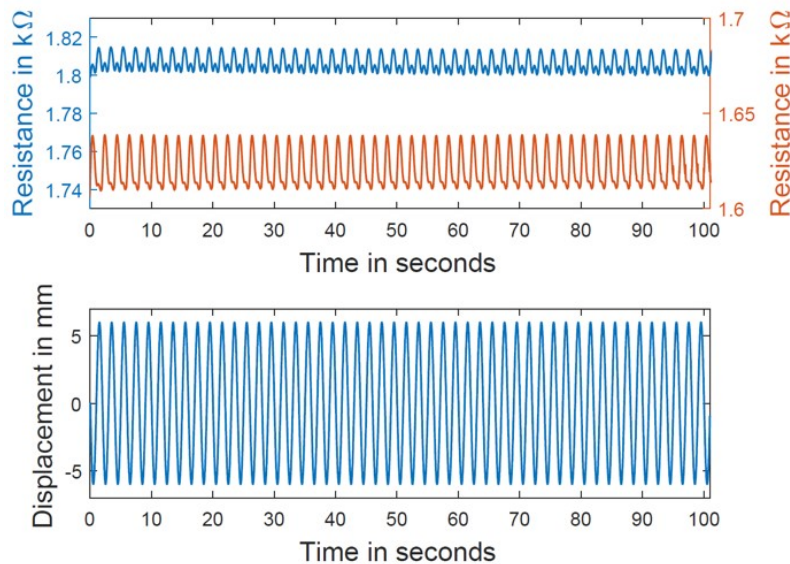


Figure 6.2: Resistance measurement

6.2.2 Drift

The second measurement that has been performed is a measurement of the drift in the sensor. Both the front and the back strain gauge have been measured while an offset of 6 mm is given for an extended period of time to the free end of the sensor. The same measurement has been performed in the opposite direction. These measurements can be observed in figure 6.3.

6.2.3 Resonance frequency

In order to see whether the flapping wings of the Robird would interfere with the sensor, the resonance frequency of the sensor is determined. The frequency of the flapping may cause vibrations in the sensor, which can interfere with the desired signal. By giving the sensor a step response, the resonance frequency can be determined from the measurements. To this end, the measurement consists of giving the SMAC actuator an offset large enough for the sensor to

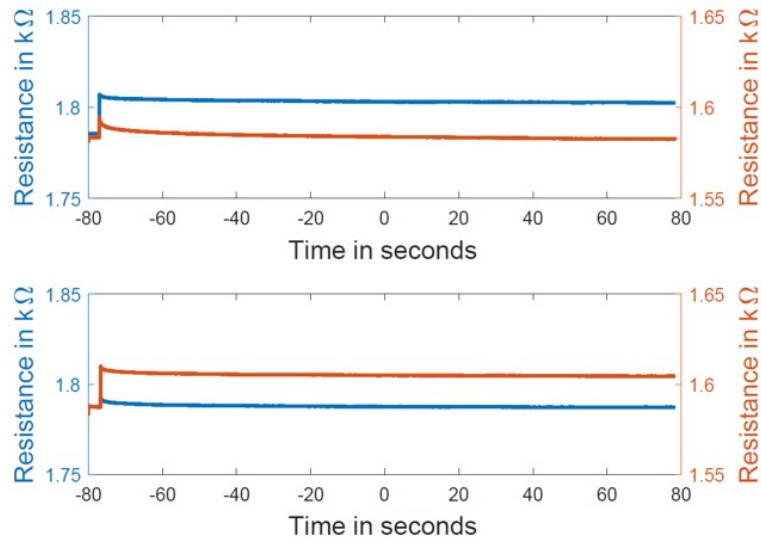


Figure 6.3: Drift measurement 6mm (top) and -6mm (bottom) displacement.

slip out of the notch where the free end of the sensor was positioned. This measurement can only be performed with an offset of -6 mm, due to the metal mount on the actuator (as seen in figure 6.1). The step response measurement is given in plot 6.4.

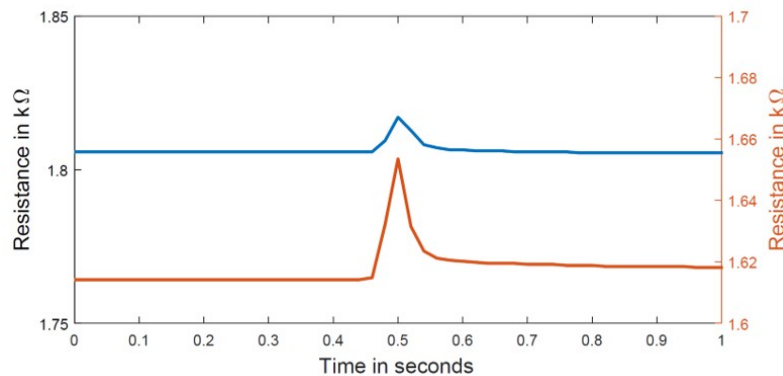


Figure 6.4: A step response measurement of both strain gauges.

When analysing the data of plot 6.4 of the step response in the strain gauges, it is clear that the sensor is either over-damped or critically damped. The expected result was an under-damped system where multiple periods were visible, but when the system is over-damped or critically damped, this period will not show in the plot.

6.3 Conclusion

The resistance of the strain gauges have been measured with a deformation of 6 mm and -6 mm with a frequency of 0.5 Hz. Together with this sinusoidal measurement, a measurement of the drift and a measurement of the oscillation frequency have been performed. This resulted in clean and interpret-able measurements.

7 Results

7.1 Introduction

In this chapter, the measurements are analysed and processed with the use of Matlab (Math-Works (2018)).

7.2 Results

In order to find the strain of the measured signal, it is important to first plot the signals as a relative change in resistance, instead of the total resistance. To do so, the following manipulation is done:

$$\frac{\Delta R_{\text{front}}}{R_{\text{front}}} = \frac{(R_{\text{front}} + \Delta R_{\text{front}}) - R_{\text{front}}}{R_{\text{front}}} = \frac{(R_{\text{front}} + 2\Delta R_{\text{front-strip}}) - R_{\text{front}}}{R_{\text{front}}} \quad (7.1)$$

$$\frac{\Delta R_{\text{front}}}{R_{\text{front}}} = \frac{2\Delta R_{\text{front-strip}}}{R_{\text{front}}} \quad (7.2)$$

Where $R + \Delta R$ is the initial measured resistance. However, as mentioned in chapter 6, the resistance that is measured is $R + 2\Delta R$, due to the fact that there are two measurement strips in each strain gauge. When this is done at both the front strain gauge and the back strain gauge, these can then be subtracted from each other to see what the overall relative change in resistance. To end up with the relative change in resistance of a single strip, the total should then be divided by 4. As shown in calculation 7.3:

$$\frac{\Delta R_{\text{tot}}}{R} = \frac{1}{4} \left(\frac{2\Delta R_{\text{front-strip}}}{R_{\text{front}}} - \frac{2\Delta R_{\text{back-strip}}}{R_{\text{back}}} \right) \quad (7.3)$$

This type of processing is possible due to the equal drift that both strain gauges experience. As seen in figure 6.3, both strain gauges have the same response to a step function in either directions. This allows for the possibility to manipulate the measurements in a differential manner, meaning that both signals can be combined as proposed in equation 7.3. The relative change in resistance can be seen in figure 7.1. When looking at this plot, the signal looks a lot like a sine. Originally, this was the foreseen result. However, when reviewing the resistance measurements of the separate strain gauges (figure 6.2), a sine-wave is not a trivial result. It appears that, even though the strain gauges do not behave as desired when they are compressed, the error is minimised because the signals are taken differential. The lower plot of figure 7.1 shows the applied strain in a single measurement strip. The applied strain is calculated using equation 4.20. In figure 7.2 a coloured plot is given for the relative resistance change with respect to the applied strain. This plot clearly shows the relation between the strain and $\Delta R/R$, but it also shows that this relation changes over time. In the first ≈ 30 s, $\Delta R/R$ appears to have a linear relation with the strain. However, after a while the figure shows signs of hysteresis. Meaning that decreasing the strain on the sensor to a certain level has a different effect than increasing the strain to this same level. The stretching of the strain gauges may affect the material properties for certain moments of time, thus creating the hysteresis effect.

A Fast Fourier Transform has been made of the measurements to be able to see whether there are more signals or interference's acting upon the sensor. This FFT is shown in figure 7.3. As can be seen in the plot, there are several peaks in the frequency domain. The largest peak is at a frequency of 0.5 Hz with a magnitude of 0.002. All frequency components together form the actual signal. Next to the main peak, there are smaller peaks visible. However, these are all located at multiples of the 0.5 Hz, meaning that these peaks represent the harmonics of the

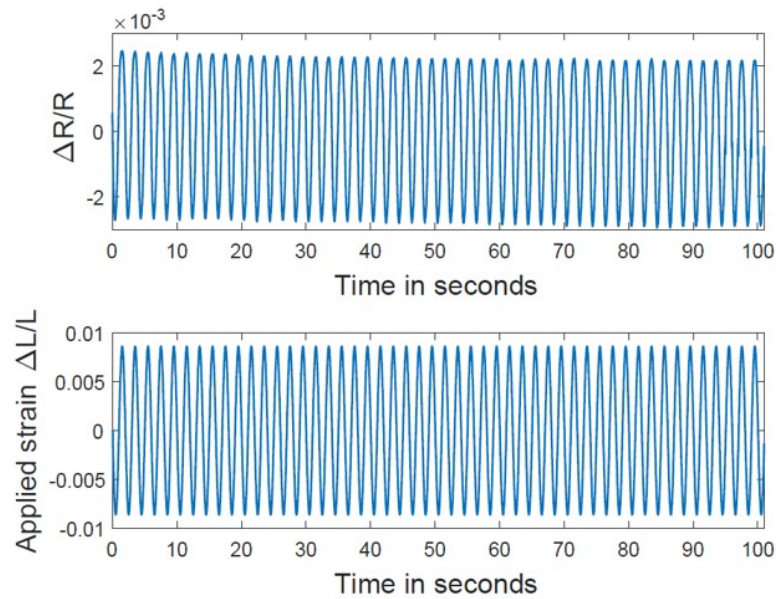


Figure 7.1: The relative change in resistance together with the combined strain.

base frequency at which the actuator was moving. With this FFT, it can be said that the signal was not affected by any outside sources or flows during the measurements.

7.2.1 Approximation

Due to the absence of concrete research results on the piezoresistive properties of PI-ETPU 85-700+ (Schouten (2017)), an approximation has to be made to translate $\Delta R/R$ to $\Delta L/L$. By taking the average magnitude of the applied strain and dividing it by the average magnitude of the resistivity $\Delta R/R$ a factor $\alpha = 3.95$ has been found. The factor α is a positive parameter, due to the fact that the resistance increases when the strain gauge becomes longer. Multiplying the measured resistivity with α , plot 7.4 is obtained. This plot gives a better view of the signal output. It becomes clear that the signal, in contrast to earlier statements, does not represent a sine-wave. When the sensor encounters a negative displacement it gives a different response than when the sensor is displaced forward. When assuming a linear relation between the resistivity and the strain, both the positive and the negative magnitude in plot 7.4 should be the same. However, the magnitude is slightly larger in the negative region than in the positive region. This is probably caused due to the uneven response of the front and the back strain gauges. Plot 7.4 can still be translated to the actual flow velocity that would be applied to the sensor. By inverting equation 4.19, v^2 can be calculated and taken the square root will leave the following equation:

$$v = \sqrt{\frac{\Delta L}{L} \cdot \frac{32EI}{(1.28)(1.225)bel(3l - L)}} \quad (7.4)$$

From this formula it is possible to plot the flow velocity. However, only the positive velocities are plotted due to the square root in this equations. The negative flow velocities are clipped to 0 ms^{-1} for now in this plot. The plot of the voltage can be seen in figure 7.5. Even though the output signal does not exactly follow the input, it does resemble the displacement given as input.

7.3 Conclusion

The measured signals from the strain gauges show a clean response. But due to the fact that the front strain gauge and the back strain gauge do not give the same response to the applied

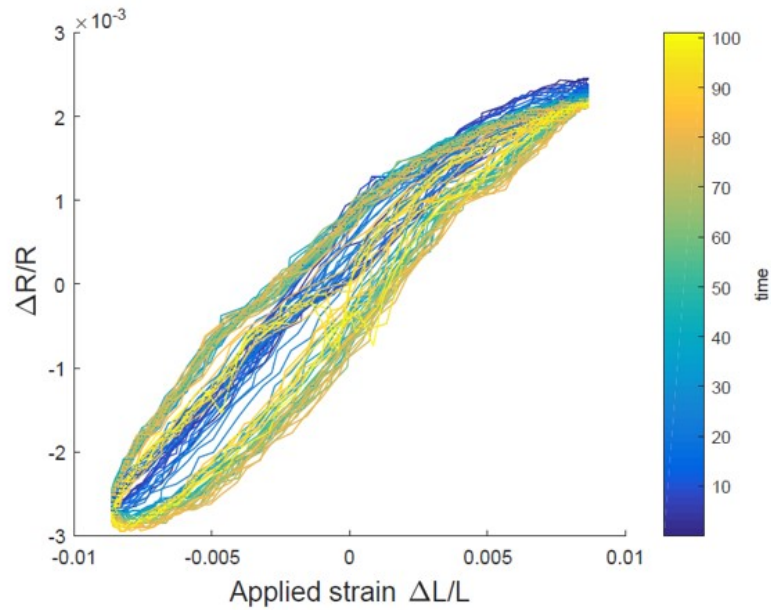


Figure 7.2: The differential relative change in resistance with respect to the applied strain and time.

strain, the processed response is not equal to the expected output. This may be caused by the fabrication of the sensor. The bottom strain gauge has been pressed firmly against a solid plate and has been heated by not only the plate, but also the additional layers of filament. This strain gauge served as part of the bottom layer of the print, thus deformed by the heat and weight of the total print. This is visually present when inspecting the sensor in figure 5.5f. The top strain gauge was immediately cooled by air and has been created at the end of the printing process. These factors may affect the equality of the response of both strain-gauges as seen when observing the measurements of the resistance in figure 6.2.

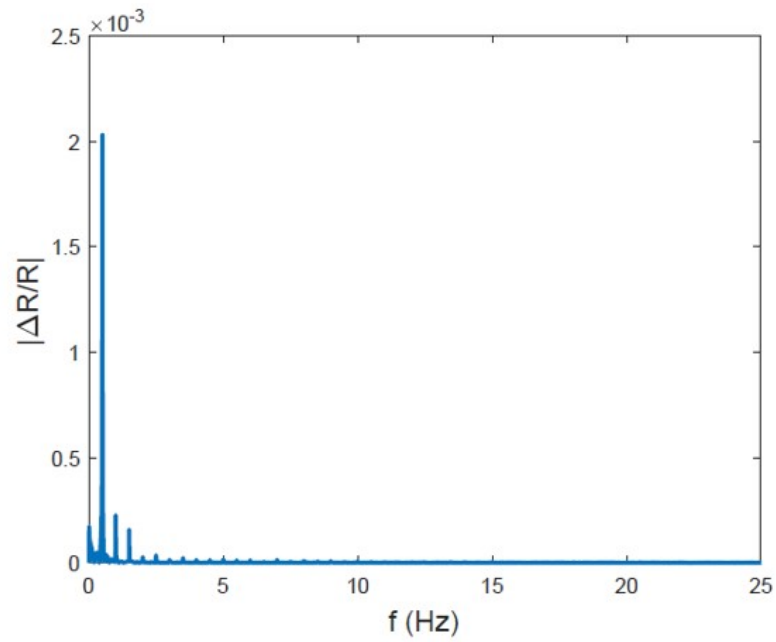


Figure 7.3: A Fast Fourier Transform of the measured relative resistance change.

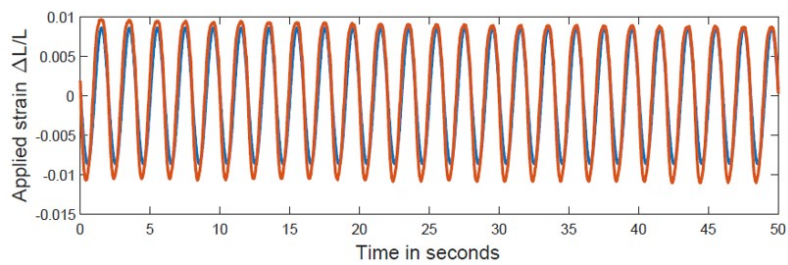


Figure 7.4: An approximation of the strain (orange) with $\alpha = 3.95$ together with the applied strain (blue).

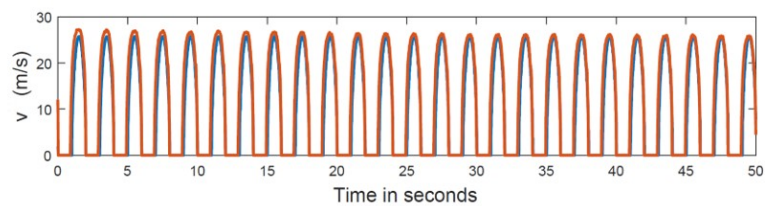


Figure 7.5: An approximation of the flow velocity (orange) with $\alpha = 3.95$ together with the applied flow (blue).

8 Conclusion

This project has shown that it is indeed possible to design a working 3D printed flow sensor. In this process, the method of 3D printing and the design of the sensor have been crucial. 3D printing brings many possibilities when it comes to sensor design, but it also introduces many issues. In order to produce a quality sample, the design should fit to the settings of the printer. The sensor was able to measure the corresponding strain and airflow, but due to the current production method it was not possible to produce a highly accurate sensor. The errors that occurred in the measurements are thought to be caused by the different conditions of the strain gauges during the printing process. As said, the strain gauge at the backside of the sensor served as part of the bottom layer of the print, therefore showing signs of deformation by the heat and weight of the total print.

9 Recommendations

Even though the relation between the resistivity and the strain can be linearly approximated, it did not result in an accurate sensor. A better approximation would be to use a polynomial approximation to translate between the piezoresistivity and the strain. However if the printing method could be adjusted, the model could be produced in a better and, most important, more symmetrical manner. Symmetrical meaning that the front strain gauge and the back strain gauge would be identical. For example, if the printer could print support materials, then underneath the back strain gauge and on top of the top strain gauge a layer of support material could be printed. This would make sure that both strain gauges undergo the same printing process and circumstances. Doing so, together with a polynomial approximation will result in a stable sensor with high accuracy. Additionally, a measurement setup with an actual wind tunnel would confirm the purpose of the flow sensor.

Bibliography

- B Eijking, R. S. and G. Krijnen (2017), *Development of Whisker Inspired 3D Multi-Material Printed Flexible Tactile Sensors*, IEEE, ISBN 978-1-5090-1012-7.
- Beer, F. P. (2013), Chapter 9.8: Product of inertia, in *Vector Mechanics for Engineers*, p. 495, ISBN 978-0-07-339813-6.
- Clear flight solutions (2018), Robird.
<https://clearflightsolutions.com/methods/robirds>
- Digilent (2018), Analog Discovery 2.
<https://reference.digilentinc.com/reference/instrumentation/analog-discovery-2/start>
- Digilent inc (2019), Waveforms.
<http://www.20-sim.com/>
- Engineerings Edge (2000), Viscosity of Air, Dynamic and Kinematic.
https://www.engineersedge.com/physics/viscosity_of_air_dynamic_and_kinematic_14483.htm
- Flashforge (2019), Flashforge Creator Pro.
<http://www.flashforge.com/creator-pro-3d-printer/>
- G Wolterink, R Sanders, F. M. B. v. B. and G. Krijnen (2017), *3D-Printing Soft sEMG Sensing Structures*, IEEE, ISBN 978-1-5090-1012-7.
- Gere, James M.; Goodno, B. J. (2012), Mechanics of Materials, in *Mechanics of Materials*, volume 6, Ed. R. J. Stenquist B, pp. 264–299, ISBN 0-534-41793-0.
- Grenander, U. (1959), in *Probability and Statistics: The Harald Cram r Volume*, Almqvist and Wiksell, doi:10.2307/3614145.
- H Droogendijk, J Casas, T. S. and G. Krijnen (2014), Performance assessment of bio-inspired systems: flow sensing MEMS hairs, IOP Publishing, doi:10.1088/1748-3190/10/1/016001.
- IPFS (2017), Density of air.
https://ipfs.io/ipfs/QmXoyvizjW3WknFiJnKLwHCnL72vedxjQkDDP1mXWo6uco/wiki/Density_of_air.html#cite_note-SInote01-13
- MakeShaper (2018), X60 60A.
<https://flexionextruder.com/shop/x60-ultra-flexible-filament-white/>
- MathWorks (2018), Matlab R2016B.
<https://nl.mathworks.com/products/matlab.html>
- Mitra Hartmann (2018), Sensory and Neutral Systems Engineering.
<http://hartmann.mech.northwestern.edu/index.php>
- NASA (2013), Shape effects on Drag.
<https://www.grc.nasa.gov/WWW/k-12/airplane/shaped.html>
- NASA (2015), The drag equation.
<https://www.grc.nasa.gov/www/k-12/airplane/drageq.html>
- NinjaTek (2018), Young’s modulus NinjaFlex.
<https://ninjatek.fppsites.com/wp-content/uploads/2018/10/tech-data-metric.pdf>
- NinjaTek (2019), Ninjaflex 85 A.
<https://ninjatek.com/ninjaflex/>

RaM (2018), ROBIRD.

<https://www.ram.ewi.utwente.nl/research/project/robird.html>

Schlichting, H. (1960), in *Boundary-layer theory Vol 7.*, p. 140, ISBN 978-3-662-52917-1,
doi:10.1007/978-3-662-52919-5.

Schouten, M. (2017), *Toward additively manufactured complex robotic systems*, RaM, Utwente,
ISBN 0123456789.

SMAC Moving Coil Actuator (2019), LAL Series Actuators.

https://www.smac-mca.com/lal-series-p-35.html?cPath=1_4